# MSDE

## PAPER

# Single-atom cobalt encapsulated in carbon nanotubes as an effective catalyst for enhancing sulfur conversion in lithium–sulfur batteries†

Khalida Abaid Samawi,[a] Ekhlas Abd-Alkuder Salman,[a] Hiba Ali Hasan,[b] HassabAlla M. A. Mahmoud,[c] Sura Mohammad Mohealdeen,[d] G. Abdulkareem-Alsultan, [iD] *[e] Emilia Abdulmalek[fg] and Maadh Fawzi Nassar [iD] *[fg]

The application of single-atom catalysts offers an auspicious resolution to the obstacles introduced by the polysulfide shuttle phenomenon and the sluggish sulfur conversion kinetics in lithium–sulfur batteries (LSBs). This research presents results regarding a sulfur host that demonstrates redox activity and resistance to polymeric sulfur species (PSS). High-curvature carbon nanotubes are utilized in the construction of a single atom $CoN_4$ catalyst through a series of steps including pyrolysis, surface processing, electrostatic adsorption, and polymerization. Undoubtedly, the presence of cobalt (Co) atoms as discrete entities was revealed by X-ray absorption spectroscopy and transmission electron microscopy, as these atoms showed dimensions consistent with the sulfur components on the cathode side. This configuration enables catalytic activity with a remarkable 100% atomic utilization functionality. Furthermore, the DFT calculation of free energy values indicates that the reduction of LiPSs on the carbon nanotube with surface curvature is more advantageous compared to the planar carbon surface. The obtained data suggest that the sulfur cathode, which was fabricated utilizing CoSAC/CNT, demonstrates electrocatalytic capability in the transformation of soluble polysulfides to insoluble $Li_2S$. As a consequence, the detrimental effects of the polysulfide shuttle effect are mitigated. The recently introduced sulfur host in the LSB exhibits consistent performance over 1000 cycles. It sustains a capacity of 990 mA h $g^{-1}$ at a rate of 1C, with a sulfur loading of 2.0 mg $cm^{-2}$. An impressive area-specific power of 4.1 mA h $cm^{-2}$ is achieved with a considerable sulfur loading of 7 mg $cm^{-2}$. This single-atom cobalt catalyst shows significant potential as a next-generation cathode material for LSBs.

### Design, System, Application

In this study, we tackle the challenges impeding the efficacy of LSBs using the application of single-atom catalysts (SACs), focusing on their potential to overcome issues related to the polysulfide shuttle phenomenon and sluggish sulfur conversion kinetics. Our innovative design centers on the integration of high-curvature CNTs as a structural matrix for the formation of single cobalt (Co) atoms ($CoN_4$), a process involving pyrolysis, surface processing, electrostatic adsorption, and polymerization. Rigorous characterization using HRTEM and X-ray absorption spectroscopy verifies the discrete nature of Co atoms, aligning precisely with sulfur species in LSB cathodes. This SAC configuration demonstrates exceptional catalytic activity, achieving 100% atomic utilization functionality. Further, DFT calculation shows the advantageous reduction of lithium polysulfides (LiPSs) on the high-curvature CNT surface compared to planar surfaces, facilitating effective electrocatalysis and transforming soluble polysulfides into insoluble $Li_2S$. The resulting sulfur cathode, denoted as CoSAC/CNT, exhibits sustained electrocatalytic capability over 1000 cycles, maintaining a capacity of 990 mA h $g^{-1}$ at a 1C rate. Impressively, an area-specific power of 4.1 mA h $cm^{-2}$ is obtained with a considerable sulfur loading of 7 mg $cm^{-2}$; the LSB cathode material demonstrates high performance based on our single Co atom catalyst. This comprehensive approach not only advances the understanding of design principles but also demonstrates practical feasibility in achieving prolonged and high-performance energy storage in LSBs.

[a] Department of Chemistry, College of Science, Al-Nahrain University, Baghdad, Iraq

[b] Department of Pharmacognosy and Medicinal Plants, College of Pharmacy, Mustansiriyah University, Baghdad, Iraq

[c] Department of Physics, Faculty of Sciences and Arts, King Khalid University, Muhayil Asir 63311, Saudi Arabia

[d] Department of Radiology & Sonar Techniques, Al-Noor University College, Nineveh, Iraq

[e] Faculty of Science and Natural Resources, Universiti Malaysia Sabah, 88400 Kota Kinabalu, Sabah, Malaysia. E-mail: Kreem.alsultan@ums.edu.my

[f] Integrated Chemical BioPhysics Research, Faculty of Science, Universiti Putra Malaysia, 43400 UPM Serdang, Selangor, Malaysia.
E-mail: nassarmaadh@gmail.com

[g] Department of Chemistry, Faculty of Science, Universiti Putra Malaysia, 43400 UPM Serdang, Selangor, Malaysia

† Electronic supplementary information (ESI) available. See DOI: https://doi.org/10.1039/d3me00191a

# Introduction

The ever-increasing human population has resulted in a dramatic increase in the need for energy, while the extensive use of fossil fuels has contributed to pollution and climate change.[1,2] For this reason, protecting our delicate ecosystem and creating reliable renewable energy sources are paramount. To do so, we must transition away from fossil fuels and towards renewable energy sources.[3] Currently, lithium-ion batteries have found widespread use in various handheld electronic gadgets.[4] However, the low power density of lithium-ion batteries (LIBs) has prevented their broad use due to an increasing need for facilities to store energy (for instance, the battery-powered car's road distance is 500 km for a single charge). For this reason, it is crucial to create future-oriented electrochemical devices for storing energy that improve upon the current generation concerning energy density, cycle duration, and affordability.[5]

Furthermore, as a promising and advanced storage system, lithium batteries have received special attention. This can be attributed to their remarkable hypothetical specific capacity of 1675 mA h $g^{-1}$ and specific energy density of 2600 W h $kg^{-1}$. With such noteworthy capabilities, it's no wonder that Li–S batteries are being touted as a promising solution for future energy needs. Despite this, the commercialization of LSBs is hindered by issues including limited areal capability, poor mass loading, and fast capacity decline during cycling.[6–15] Considering the non-conductive structure of both sulfur and the discharged intermediates ($Li_2S_2$ and $Li_2S$) towards electrons ($e^-$) and lithium ions ($Li^+$), the dynamics of the transformation process are constrained, leading to limited exploitation of sulfur.[16–20] The generation of Li polysulfides during the conversion reaction is known to result in solubility in frequently employed organic electrolytes for lithium–sulfur batteries.[21] This solubility results in many detrimental effects, such as the "shuttle effect," as well as poor coulombic efficiency, rapid capacity decline, and a high self-discharge ratio. The density of $S_8$ is higher than that of $Li_2S$ (1.66 g $cm^3$). As a result, the process of lithiation leads to a substantial expansion in volume, amounting to an 80% increase.[8,22] Moreover, lithium dendrites, changes in the volume and shape of the lithium anode, metallic Li anode cracking, and instability in the solid electrolyte interphase (SEI) are some of the disadvantages of using lithium as an anode electrode.[23] Over the past decade, researchers have poured time and energy into studying Li–S batteries and have offered several solutions to the problems listed above.[24–26]

Chemical attachment and lithium polysulfide (LiPS) transformation promotion were two methods previously studied to improve the cathodic component and avoid the shuttle effect for optimum efficiency.[27] In Li–S batteries, it is necessary to reduce the shuttle effect of polysulfide by producing some new materials such as metal sulfides (MS), metal oxides (MO), N-doped porous carbon, etc. as new sulfur hosts.[28–31] Nevertheless, increasing the weight ratio of bulk metal-based elements in Li–S batteries leads to a decrease in energy density.[9,12,14,30,32–37]

Due to their exceptional catalytic characteristics and boosted metal exploitation efficiency, single-atom catalysts (SACs) with fundamentally distributed metal atoms attached to appropriate scaffolds have received significant attention for an extensive variety of energy and chemical conversion processes.[38–40] At present, the research and development of SACs for their potential use in lithium–sulfur batteries is still in its early stages.[41–43] Various SACs with different local atomic structures and frameworks, especially M–N₄ and M–O₄ centers, have been employed in lithium–sulfur batteries. Li et al.[44] reported a cobalt SAC supported on N-doped carbon, and their obtained results show that the fabricated catalyst is active toward LiPS conversion.[45] In another work, Meng and coworkers prepared a cathode catalyst based on single Co atoms supported on graphene and investigated the effect of the atomic aggregates' size on catalytic activity toward LiPS conversion.[46] These SACs have shown extraordinary efficacy in preventing lithium dendrite development and facilitating the catalytic conversion of polysulfides.[39,45,47] Some carbon-based composites with atomically scattered metal ions have been studied for their potential as a LiPS conversion mediator. However, despite the notable benefits that SACs provide, certain aspects necessitate enhancement. Importantly to indicate that the agglomeration of metal atoms occurs due to their elevated surface energy on the catalyst surface. This can lead to the creation of clusters, which have the potential to reduce the overall catalytic performance. It is crucial to confront this obstacle to advance the functionality and dependability of SACs utilized in energy transformation systems. For this reason, the development of a durable substrate capable of supporting single metal atoms is critical to the progress and effectiveness of SACs. Despite the advantageous characteristics of high dispersion and large surface area, the contribution of the planar support to the enhancement of the catalytic process is negligible.[48] Materials with curved surfaces like the catalyst materials of Li–S batteries present novel opportunities for investigating and improving the characteristics of SACs in a variety of catalytic applications.[49–53] A study of the fundamental relationship between structure and properties is critical to identifying the parameters that have a substantial impact on electrocatalytic activity. Computational investigations such as molecular dynamics (MD) and density functional theory (DFT) have confirmed the presence of a ragged surface in catalysts. This surface leads to an irregular arrangement of charges and facilitates the formation of strain effects.[54] Changing the surface curvature of catalysts or designing new catalysts with a novel surface curvature was shown to improve catalytic activity.[54,55] The development and fabrication of a substrate featuring an exceptionally curved configuration to accommodate SACs may represent a viable strategy for enhancing catalytic performance. To optimize the battery's efficiency, it is preferable to employ materials with a high concentration of single metal atoms, providing a substantial number of reactive sites. In this study, we developed and implemented a multi-step method for the synthesis of Co–N₄ SACs on high-curvature carbon nanotubes (CNTs) using polymerization, surface treatment, electrostatically induced

adsorption, and pyrolysis. The $Co-N_4$ SACs/CNT catalysts show promising performance toward polysulfide conversion. The built Li–S battery comprising the $CoN_4$@CNT cathode material had a notable starting capacity of 1346 mA h $g^{-1}$. Subsequently, after undergoing 1000 cycles with a rate of 1C, the battery's overall capacity decreased to 990 mA h $g^{-1}$. Moreover, the free energy values obtained from DFT calculation show that the CNT curved surface is more favorable for the polysulfide conversion reaction than planar carbon surfaces.

## Experimental

### Preparation of $MnO_2$ nanowires

The long $MnO_2$ nanowires were produced using a hydrothermal method. By dissolving 6 mg of manganese sulfate ($MnSO_4$), 4 mg of $KMnO_4$ and 4 mg of $NH_4F$ in 40 mL of DI water with magnetic stirring, a homogeneous solution was obtained. The reaction mixture was subsequently introduced into a 100 mL stainless steel autoclave equipped with a Teflon liner and maintained at 160 °C in an oven for 13 hours. The brown product was extracted after the autoclave had self-cooled to ambient temperature. While subjecting it to ultrasonic waves, 100 mg of the newly prepared product was suspended in 100 mL of distilled water. The monomers pyrrole (0.8 mL) and aniline (0.6 mL) were individually dissolved in 100 mL of 0.1 M $H_2SO_4$ solution.

### Preparation of the polypyrrole/polyaniline copolymer (PPy/PANI copolymer)

The pyrrole/aniline mixture was vigorously stirred with the prepared $MnO_2$ NW dispersion for 15 minutes, resulting in a black substance after four hours of reaction. The product was then rinsed and dried.

### Preparation of $CoN_4$SACs/CNT (CoSAC@CNT)

The preparation of the catalyst involved dispersing 100 mg of sodium dodecyl benzene sulfonate (SDBS) and 400 mg of PPy/PANI copolymer in 40 mL of DI water. For six continuous hours, the reaction mixture was stirred, and then 60 mg of $CoCl_2 \cdot 6H_2O$ was incorporated. The obtained crude product was rinsed several times with a solvent system of ethanol and DI water and then dried after being stirred for 12 hours. For the final step, the black product was positioned in a nitrogen-filled environment and heated to 850 °C for 10 hours to undergo carbonization (Scheme 1).

### Fabrication of CoNP@CNT

To compare the catalytic activity of Co single atoms and Co nanoparticles, Co nanoparticles were supported on CNTs using the incipient wetness impregnation method, as described in ref. 56.
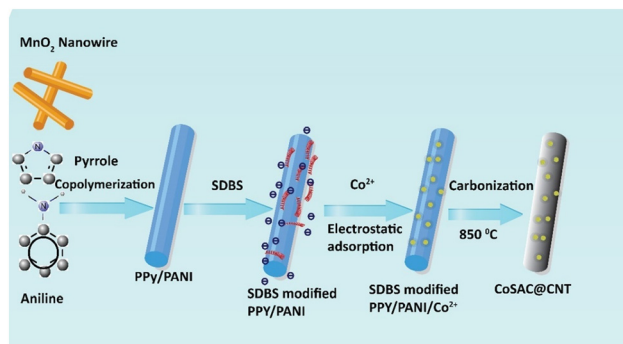


**Scheme 1** Preparation process of CoSAC@CNT.

### Fabrication of CoSAC@CNT/S

CoSAC@CNT and sulfur powder were homogenized in a 2 : 3 mass ratio using a milling technique. Subsequently, the concoction was subjected to a temperature of 155 °C for 12 hours within a tightly sealed container that was saturated with argon gas. Using the same procedure, the composites of CNT/S and CoNP@CNT/S were produced as well.

### Fabrication of the cathode electrode

To prepare the sulfur electrode, a sulfur slurry (consisting of 80 wt% CoSAC@NCNT/S, CoSAC/S, and NCNT/S as the active component, 10 wt% super P, and 10 wt% PVDF binder) was applied onto an aluminum foil collector. After being coated with the slurry, the aluminum foil was vacuum-dried overnight at 60 °C. Subsequently, the sulfur electrodes were sectioned into round pieces and employed as functional active electrodes.

### Cell assembly

The experimental setup involved the assembly of coin cells (specifically CR 2032) within a glovebox filled with argon gas. A lithium sheet served as the anode material, with Celgard 2400 serving as the separator. The mixture solution consisting of dimethoxymethane (DME) and 1,3-dioxolane (DOL) in a 1 : 1 ratio was combined with the electrolyte which consists of 1 M LiTFSI (lithium bis(trifluoromethanesulfonyl) imide) solution with an additional 2.0% concentration of $LiNO_3$. Hence, the mass proportion of sulfur in the composite electrode is calculated as (80% × 75.5%) resulting in a value of 60.40%. The identified ratio between sulfur and electrolyte was about 15 μL $mg^{-1}$ with loading (areal sulfur) values ranging between 1 and 2 mg $cm^{-2}$. Moreover, the measured surface area of the electrode was 1.15 $cm^2$ along with a diameter of 12 mm. The electrode's sulfur loading ranged from around 1.0 to 2.0 mg $cm^{-2}$. Approximately 1.0 and 2.0 mg $cm^2$ of sulfur was loaded onto the electrode.

### Electrochemical analysis

An AutoLab potentiostat was employed for the galvanostatic charge–discharge experiments. The tests were conducted at a

voltage between 1.8 and 2.9 V, at a temperature of 25 °C. Experiments using cyclic voltammetry (CV) were conducted at a scan rate of 0.1 mV s⁻¹. With a potentiostatic amplitude of 5 mV, electrochemical impedance spectroscopy (EIS) measurements were carried out over a frequency range of 100 kHz to 0.1 Hz.

**Lithium sulphide adsorption test**

Lithium sulphide (Li$_2$S) and sulphur (S) were mixed in a glove box with argon gas at a 5:1 molar ratio. The breakdown occurred in a solution made up of a 1:1 volume ratio mixture of 1,2-dimethoxyethane (DME) and 1,3-dioxolane (DOL). As a result, a solution of lithium polysulfide (Li$_2$S$_6$) was formed. Next, the Li$_2$S$_6$ solution was stirred at 80 °C. Following this, 10 mg each of CNT/S, CoNP@CNT/S, and CoSAC@CNT/S was then introduced into the solution.

**Fabrication of Li$_2$S$_6$ symmetric cells and study of polysulfide conversion kinetics**

Assembling symmetric cells involved coating Al foil with a slurry of CoSAC@CNT/S, CoSAC/S CNT/S, and PVDF in NMP with a weight proportion of 80:20 and then drying the coated foil overnight at 80 °C in a vacuum oven. Working electrodes were then formed from pellets of CoSAC@CNT/S, CoNP@CNT/S, and CNT/S electrodes that had been shaped afterward using a circular pellet cutter. CoSAC@CNT/S, CoNP@CNT/S, and CNT/S have an areal loading of roughly 1 mg cm⁻². After that, 45 µL solution of 0.2 M Li$_2$S$_6$ was placed in a conventional 2032 coin cell with two similar electrodes and a Celgard 2400 separator. Additionally, symmetrical cell analysis was conducted using cyclic voltammetry (CV) at voltages varying between −1.0 V and 1.0 V with a scanning rate of 10 mV.

**Investigation of Li$_2$S nucleation**

Preparation of the cathode was performed by mixing Li$_2$S and S in a 1:7 mole ratio which was stirred into the Li–S electrolyte to form a 0.2 M Li$_2$S$_8$ solution. The anode, consisting of metallic lithium, was placed on an Al current collector. The working cathode, also on an Al current collector, was fabricated using the same CoSAC@CNT/S, CoNP@CNT/S, and CNT/S materials as those employed in the previously described kinetic study. After applying the cathode mixture, which contained Li$_2$S$_8$ at a concentration of 0.2 M, meticulously to the cathode, 15 µL of control anolyte without Li$_2$S$_8$ was dropped on the side of lithium anode. The cells were held at a potential of 2.05 V using a potentiostatic method until the current dropped below 105 A. The discharging of cells at 2.06 V at a current of 0.10 mA leads to nucleation of Li$_2$S. To determine the kinetics of Li$_2$S formation and growth, the total charge was measured using Faraday's law.

**Investigating the structure and properties of materials**

The crystallographic orientation and phase determination of the prepared hybrid structures were determined using an X-ray diffractometer. The chemical makeup, degree of gradation, and crystal structure of materials have all been examined using Raman spectroscopy. Investigation of the morphology and crystalline structure of the composite was performed using both field-emission scanning electron microscopy (SEM) and transmission electron microscopy (TEM). The hybrids' sulfur content was measured in nitrogen using a thermogravimetric analyzer. To examine each element's chemical environment, X-ray photoelectron spectroscopy was employed to look into the chemical surroundings of each element. In order to gain an understanding of how the components coordinate at the atomic level, both EXAFS (extended X-ray absorption fine structure) and XANES (X-ray absorption near-edge structure) were conducted.

# Results and discussion

CoSAC@CNTs manifest a distinct one-dimensional hollow cylindrical structure characterized by an outer layer thickness of ≈10 nm and an internal diameter of ≈25 nm (Fig. 1a and b). The absence of Co particles or clusters in the TEM images is aligned with the nonattendance of crystal patterns specific to cobalt in the XRD pattern (Fig. 2b). Conversely, the graphitic carbon arranged in layers showcases an interplanar space of 3.40 Å, which corresponds to the crystal plane denoted as (002) (Fig. 1c). HAADF-STEM
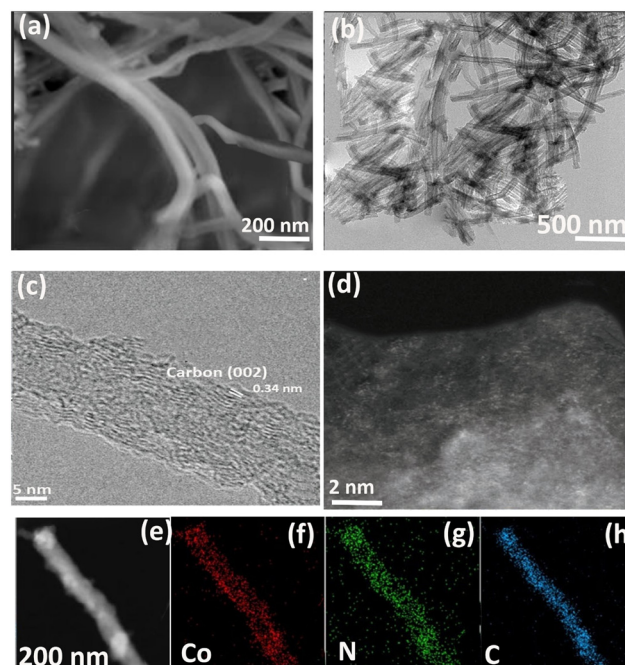


**Fig. 1** (a) SEM, (b) TEM, (c) HRTEM and (d and e) HAADF images of CoSAC@CNT, respectively, and the corresponding elemental distributions of (f) Co, (g) N and (h) C.
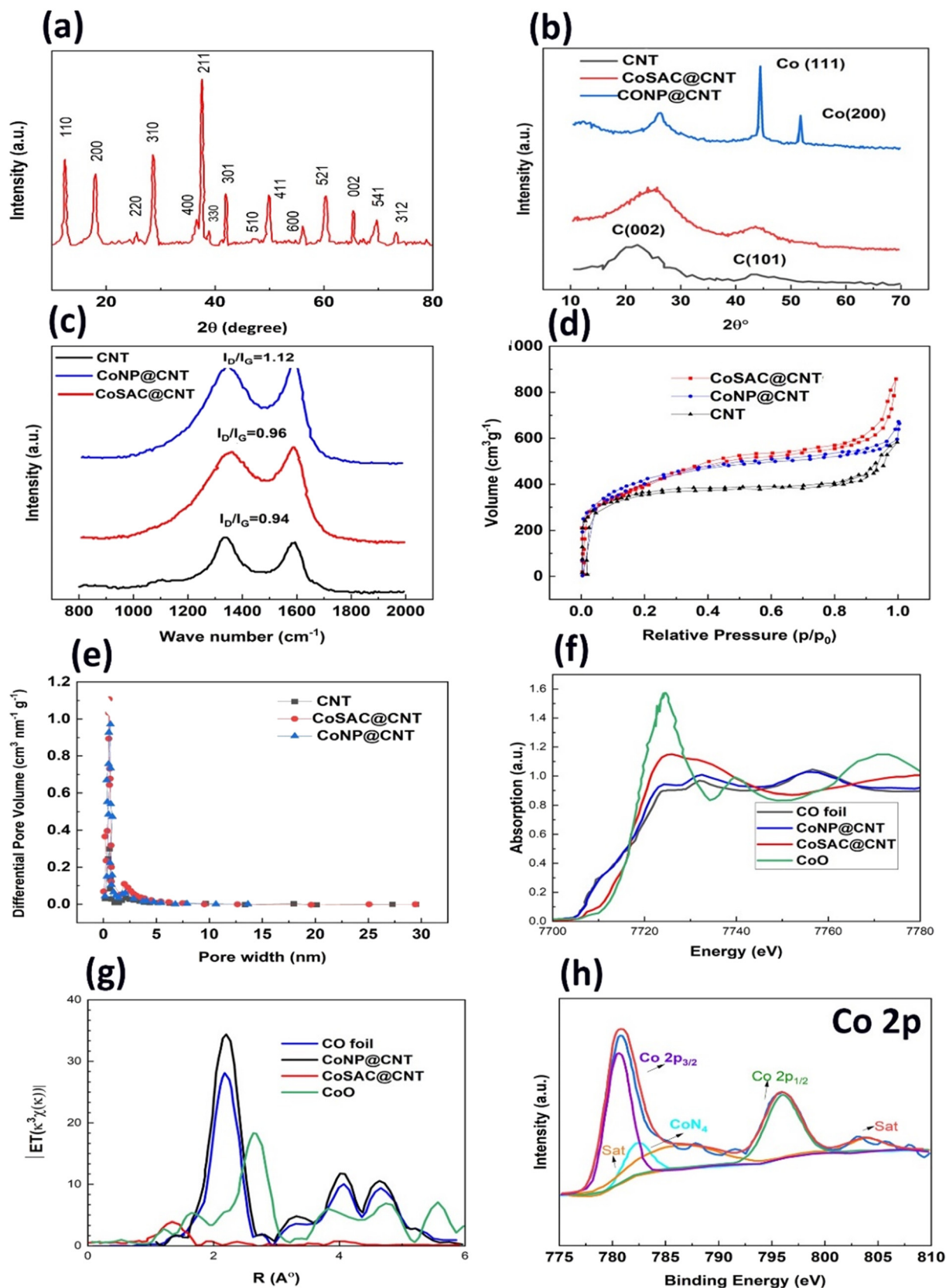
**Fig. 2** XRD patterns of (a) $MnO_2$ NW, (b) CoSAC@CNTs, CoNP@CNTs, and CNTs; (c) Raman spectra of CoSAC@CNT, CoNP@CNT, and CNTs; (d) $N_2$ adsorption–desorption isotherm curves, (e) pore size distribution of fabricated structures, (f) XANES spectra, and (g) Fourier transform (FT) of the K-edge CoSAC@CNTs, CoNP@CNTs; (h) high-resolution XPS Co 2p spectra of CoSAC@CNTs.

microscopy reveals that the bright spots are associated with the carbon support, indicating the uniform dispersion of isolated CO single atoms (Fig. 1d and e).

Phase analysis reveals the structural and compositional changes in the material. The XRD patterns of $MnO_2$ NW are displayed in Fig. 2a. $MnO_2$'s signature peaks are present exclusively, suggesting highly pure $MnO_2$ creation. For CoSAC@CNT, only the graphitic carbon diffraction patterns are seen (Fig. 2b), but for CoNP@CNTs, two additional peaks are seen that correspond to the (111)/(200) crystal face of the Co nanoparticles. CoSAC@CNT does not contain significant amounts of Co atoms or nanoparticles because there is no diffraction evidence indicating such aggregation.[57]

Raman spectroscopy was employed to characterize the three prepared samples, CoSAC@CNTs, CoNP@CNTs, and CNTs (Fig. 2c). The D and G-band peaks of these catalysts showed the expected line shapes, indicating the presence of carbon support cores. Interestingly, different intensity ratios of the D-band to G-band suggest that the degree of graphitization varies among the samples. This discrepancy might be ascribed to the incorporation of an atomic cobalt hybrid structure, which has higher crystallinity than CoNP@CNTs. As a result, the final product, CoSAC@CNTs, exhibits improved electrical conductivity.

The texture and porosity of the created samples were additionally assessed through BET analysis, revealing a substantial quantity of pores within the fabricated samples, leading to a notable specific surface area. A distinct type IV hysteresis loop is obtained from the BET analysis of the materials. The CoSAC@CNTs present a notable surface area ($S_{BET}$) of 920.15 $m^2$ $g^{-1}$, surpassing the reported values of other Co-containing catalysts from previous studies.[58,59] As per computations based on the density functional theory (DFT) methodology, the material has an average pore size of 9.7 nm and an overall pore volume of 1.4 $cm^3$ $g^{-1}$. The process of pyrolysis plays a role in controlling the specific surface area and porosity of substances. The CoSAC@CNT is a great option for obtaining remarkable catalytic performance because of a number of features. These include a clearly defined configuration and a higher pore concentration. Larger surface areas are usually directly correlated with higher activity levels. Because surface area affects the density of active sites in a material, it directly affects the substance's performance. The overall performance of the material is impacted by a higher active site density that results from an increase in surface area.

To obtain a thorough understanding of the atomic structures of the produced samples, XAFS was performed. This study used cobalt foil and cobalt oxide (CoO) as references. The CoNP@CNT sample is mostly made up of CoO, according to the X-ray absorption near-edge structure (XANES) study at the Co K-edge, while the CoSAC@CNT sample is mainly made up of $Co^{2+}$ (Fig. 2f).[60] As illustrated in Fig. 2g, the Fourier transform of the extended X-ray absorption fine structure (EXAFS) can be used to identify the atomic neighbourhood of the Co atom. The presence of a

peak at a distance of 1.5 Å in all catalysts can be ascribed to the scattering routes of Co–N. The CoSAC@CNT exhibits the most pronounced Co–N signal, with clumps and nanoparticles displaying progressively weaker signals in that order. The presence of the Co–Co peak at a distance of 2.1 Å is not observed in the CoSAC@CNT material. However, a small peak is discovered for clusters, whereas nanoparticles exhibit a very high peak.

To determine the quantifiable structural properties surrounding center atoms, a curve fitting approach utilizing the least-squares principle was employed for the EXAFS analysis. The fitting parameters used are presented in Table S1,† while the related fitted plots are shown in Fig. 2g and S1.† The coordination number of cobalt in CoSAC@CNT is approximately 4, with an average bond length of 1.88 Å. The backscattered atoms are carefully analyzed by performing a wavelet transform (WT) on the Co K-edge EXAFS oscillations, possessing high spatial resolution in real space (radial distance) and high momentum resolution in reciprocal space (K space). According to Fig. S2† and the WT counter spectra of Co foil and cobalt phthalocyanine (CoPc), the highest point of intensity at 6 and 8 was attributed to the Co–N and Co–Co species, respectively, and CoSAC@CNT exhibited a single WT maximum at 6 Å$^{-1}$, as illustrated in Fig. S2,† whereas nanoparticles only exhibited a WT maximum at 8 Å$^{-1}$. The results indicate that Co–N coordination is present exclusively in CoSAC@CNT, whereas Co–Co coordination prevails in CoNP@CNT. To shed further light on the chemical state and bonding environment of the nitrogen atoms incorporated into the carbon structure of the CoSAC@CNTs, we employed XPS analysis. As shown in Fig. S3,† three key elements were found to correspond to the N 1s spectra of both CoSAC@CNT and CoNP@CNT catalysts: pyridinic N (398.8 eV), and pyrrolic N (400.9 eV).[61] In addition, CoSAC@CNT shows an extra peak at 399.9 eV, which corresponds to Co–N moieties.[62] The Co 2p spectra confirm that the valence state of cobalt is consistent with the XANES observations in Fig. 2g. The Co–N moieties exhibit distinct peaks at approximately 782.5 eV, as observed in Fig. 2h. Additionally, the absence of a metallic Co peak in CoSAC@CNTs offers additional proof of the presence of atomically dispersed Co atoms.[63,64]

To verify the strong immobilization capability of fabricated catalyst materials towards LiPSs, we conducted an optical observation by immersing equal amounts (5 mg) of COSAC@CNT, CONP@CNT, and CNT hosts into a 3 mM $Li_2S_6$ solution in a 1:1 volume ratio of DOL and DME for 6 hours. Interestingly, the solution in the bottle containing CoSAC@CNTs was observed to be colorless, according to Fig. 3a. Conversely, color was preserved to varying degrees in solutions containing CoNP@CNT and CNTs, showing that CoSAC@CNTs have the highest ability to adsorb LiPSs. UV spectrophotometry was used to analyze the aforementioned solutions, and the findings matched those of $Li_2S_6$ adsorption tests. To conduct a more comprehensive analysis of the valence states, surface chemical nature, and
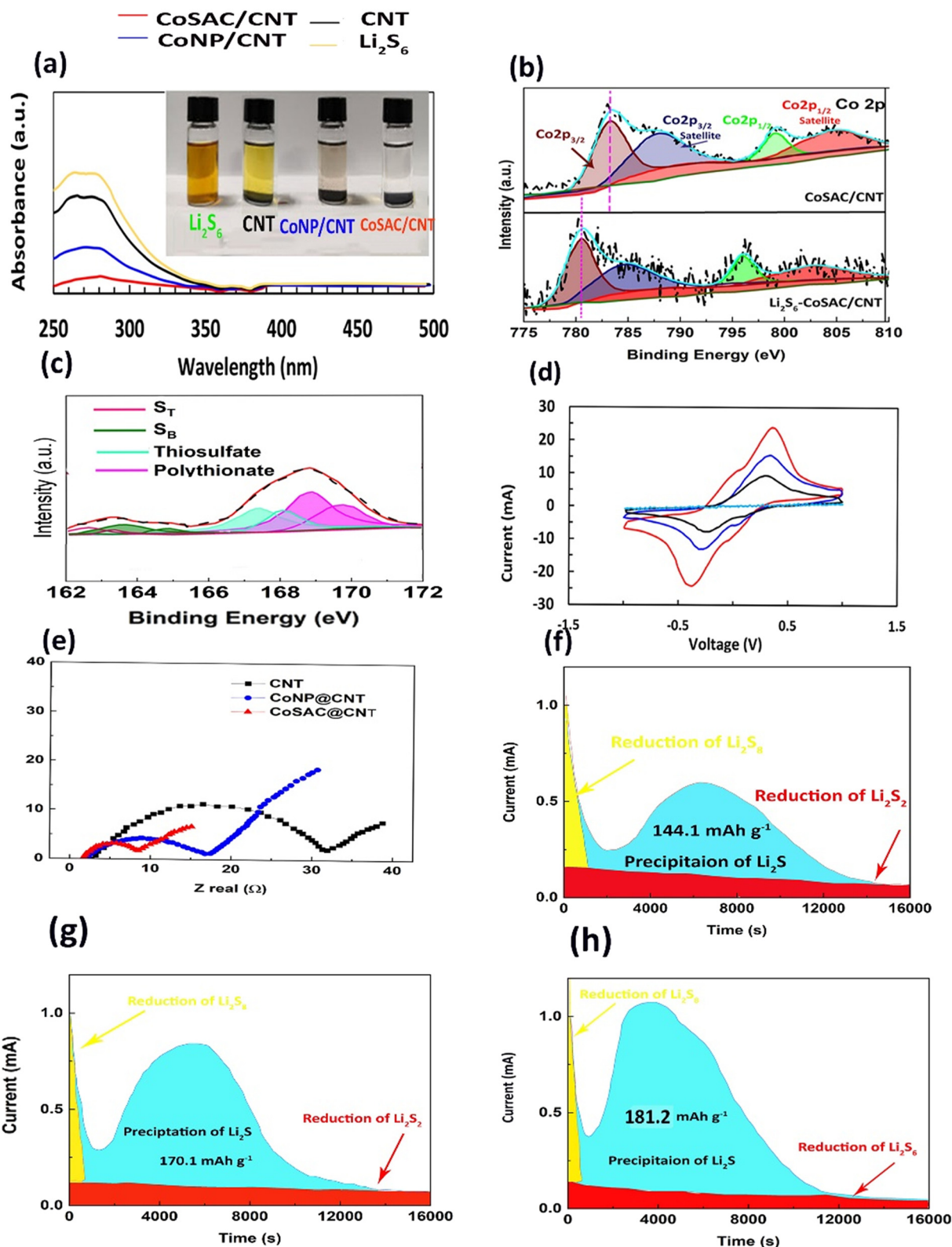
**Fig. 3** (a) Adsorption experiment on $Li_2S_6$ and its UV-vis spectra after a six-hour soak in 10 mg of CoSAC@CNTs; (b) Co 2p high-resolution XPS spectra of CoSAC@CNT before and after $Li_2S_6$ adsorption; (c) S 2p high-resolution XPS spectra of S 2p CoSAC@CNT /$Li_2S_6$; (d) CV curves of symmetric cell CoSAC@CNT at 0.1 mV s$^{-1}$ from 1.8 to 3.9 V (*vs.* Li$^+$/Li); (e) Nyquist plots of CoSAC@CNT, CoNP@CNT, and CNTs. Potentiostatic discharge curves of (f) CNTs, (g) CoNP@CNT, and (h) CoSAC@CNT.

interaction between CoSAC@CNTs and LiPSs, the CoSAC@CNT sample was subjected to XPS analysis following the adsorption of $Li_2S_6$. The status of Co 2p before and after adsorption of $Li_2S_6$ has been examined using XPS, as shown in Fig. 3b. Before conducting the $Li_2S_6$ absorption examination, the XPS analysis revealed that the Co $2p_{3/2}$ peaks were observed at an energy level of 783.3 eV, accompanied by a satellite peak at 787.6 eV.[65,66] These findings suggest the prevalence of $Co^{2+}$ species within the CoSAC@CNT sample. Following the adsorption of $Li_2S_6$, the binding energy of Co experienced a downward shift towards the lower energy area, with a magnitude of around 2.7 eV. The observed result can likely be related to the establishment of a Co–S attachment interaction, as shown by previous studies.[67,68] These results provide additional evidence for the chemical attachment impact of CoSAC@CNTs on LiPSs. The S 2p spectra (Fig. 3c) of CoSAC@CNTs/$Li_2S_6$ exhibit two distinct peaks at 161.9 and 164.1 eV. These peaks are ascribed to the existence of "terminal" ($S_T$) and "bridging" sulfur ($S_B$) derived from polysulfides, respectively.[69] The peaks detected within the binding energy range of 166 to 172 eV display greater intensity and may be well described by the existence of two different sulfur species. During fitting analysis, both detected peaks at 168.1 and 168.4 eV are ascribed to the existence of thiosulfate that is bound to the surface. The oxidation process of sulfur species which is derived from polysulfides is responsible for the spotted peaks.[70] The presence of peaks at 169.1 and 170.1 eV in the spectrum suggests the existence of a polythionate structure, which is formed through the interaction of anchored thiosulfate and polysulfides, as previously described in ref. 71. Consequently, the polythionate complex is formed through the insertion of polysulfides into the SS link of thiosulfate. Also, minimization of the shuttle effect is achieved through the transformation of soluble polysulfides ($Li_2S_x$, where $x < 4$) to a less soluble intermediate polythionate structure and shorter polysulfides ($Li_2S_y$, where $y < 3$). The aforementioned procedure efficiently confines the polysulfides, leading to improved efficiency.

To facilitate a more thorough investigation into the impact of host materials on the redox processes of lithium polysulfides (LiPSs), three specifically manufactured samples have been utilized as the electrode constituents inside a symmetric cell configuration. As against other materials looked at for battery applications, the data in Fig. 3d show that the CoSAC@CNT material exhibits the highest current density. This implies that in the context of lithium–sulphur (Li–S) batteries, the CoSAC@CNT material exhibits exceptional redox kinetics and improved catalytic properties for the conversion of LiPSs. Following the galvanic discharge within the cells, a potentiostatic discharge was applied at a voltage of 2.05 V to initiate the $Li_2S$ deposition process. More substantiation of the fact that the CoSAC@CNT electrode has the lowest charge-transport resistance may be found in the EIS spectra shown in Fig. 3e. The time-dependent decreases in current curves observed in cells made with different
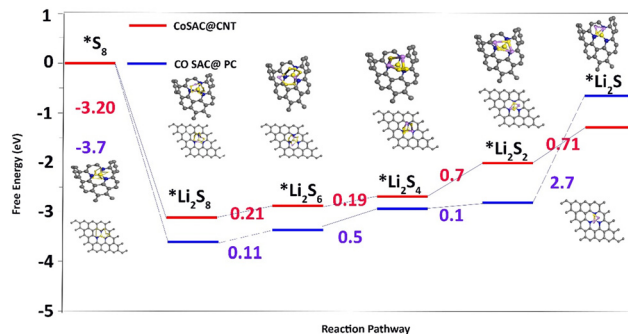


**Fig. 4** The energy level calculated using DFT for reduction of LiPSs on Co SACs incorporated in curved CNTs and planar carbon.

electrodes are shown in Fig. 3f–h. It has been noted that after a steady decrease in electrical current during the first stage, a noticeable peak appears, which is attributed to the electrodeposition of $Li_2S$. Furthermore, density functional theory (DFT) calculations were implemented to provide additional insight into the reduction mechanism of LiPs on $CoN_4SAC$. We constructed two models (CoSAC@CNT (a carbon support with a curved surface) and COSAC@PC (a carbon support with a planar surface)) to evaluate how the carbon support curvature effects the LiPS reduction process (Fig. 4). The process by which $S_8$ is reduced to $Li_2S_8$ involves an exothermic reaction that occurs spontaneously on all substrates. In contrast, the subsequent conversions ($Li_2S_8 \rightarrow Li_2S_6 \rightarrow Li_2S_4 \rightarrow Li_2S_2 \rightarrow Li_2S$) all occur at an endothermic rate. The enhanced conversion rates of lengthy polysulfides are indicated by the fact that the Gibbs free energy associated with the transition in the solubility region of polysulfides ($Li_2S_8 \rightarrow Li_2S_6 \rightarrow Li_2S_4$) is more thermodynamically favorable for CoSAC@CNT (0.5 eV).

By applying cyclic voltammetry (CV), the catalytic efficiency of synthesized compound towards sulfur conversion was determined. The CV curves of the Li–S cell at 0.1 mV $s^{-1}$ for several samples are displayed in Fig. 5a. In each sample, the signature redox signal was recovered, indicating the presence of a sulfur-based redox process. It is interesting to note that the cells associated with CoSAC@CNT have the highest peak intensities, followed by CoNP@CNT and then the bare CNT. Higher peak intensities reflect quicker rates of the associated redox processes. The CoSAC@CNT exhibits higher starting potential and maximum voltage for the reduction peaks (I and II) compared to the other fabricated electrodes, suggesting a greater favorability of the reduction reaction. On the other hand, the preceding emergence of the current response affirms that the energy threshold necessary for the reduction of sulfur compounds is diminished. It has been demonstrated that CoSAC@CNTs exhibit ideal catalytic activity for the reduction of $Li_2S$ to S, as evidenced by its peak (III) location in the reverse oxidation reaction. Tafel plots (Fig. 5b) were additionally employed to quantitatively determine the catalytic activity of CoSAC@CNTs. The calculated Tafel slopes of peak II were 31.2, 36, and 42 mV $dec^{-1}$ for CoSAC@CNT,
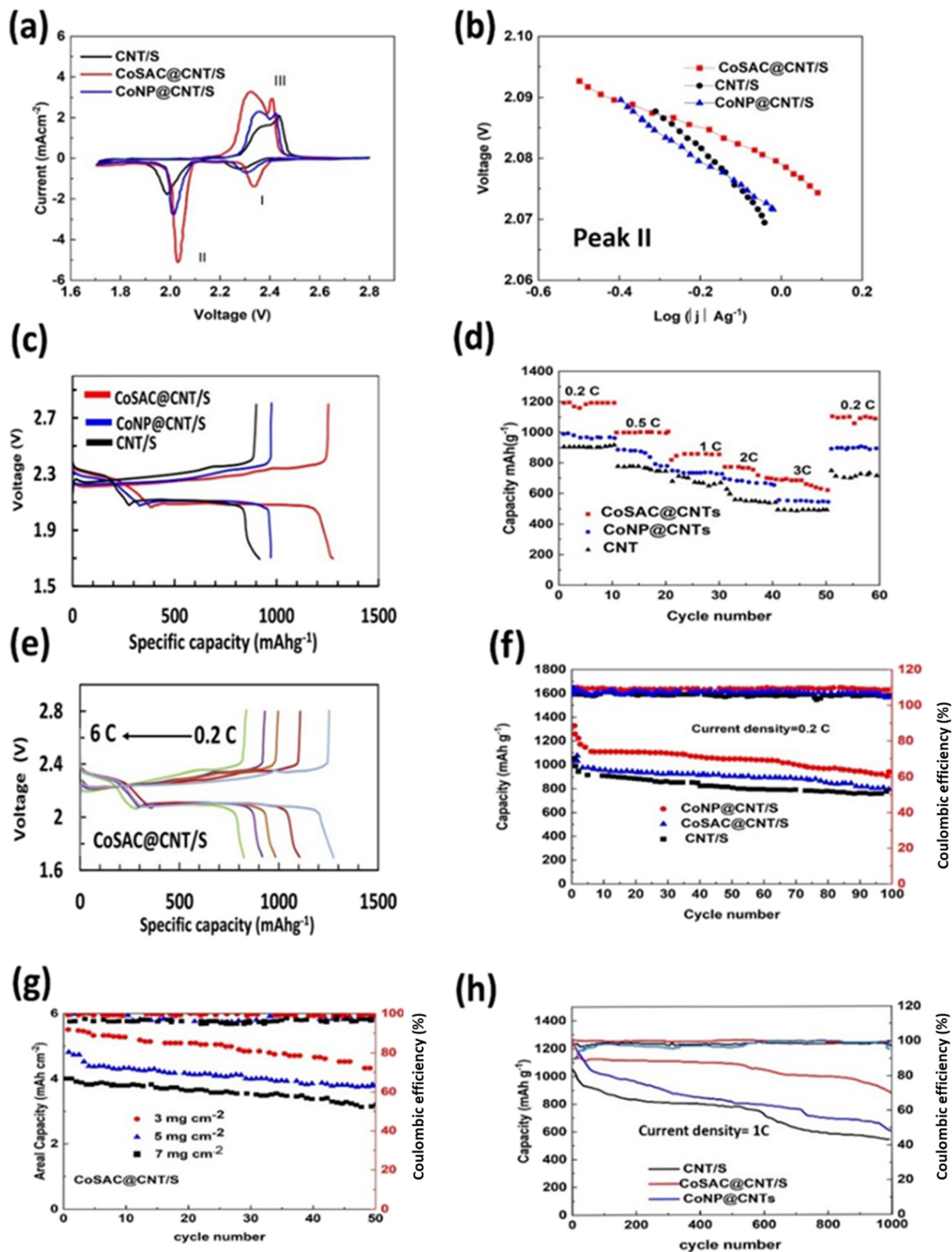
**Fig. 5** Electrochemical properties of fabricated Li–S cells. (a) CV curves obtained at a scan rate of 0.1 mV s$^{-1}$ for various cathode materials, (b) Tafel plots of peak II, (c) charge/discharge curves obtained at 0.1C for various cathode materials. (d) Rate abilities recorded for different cathode materials. (e) Charge/discharge profiles of CoSAC@CNT/S electrodes recorded at 0.2C, 1C, 2C, 3C, and 6C. (f) Cycling examination obtained at 0.2C for fabricated cells. (g) Cycling analysis obtained at 0.1C for Li–S cells fabricated using CoSAC@CNT at different sulfur loadings. (h) Cycling examination was obtained at 1C for fabricated cells. The respective legends provide information about the materials examined.

CoNP@CNTs, and CNTs, respectively, demonstrating the rapid redox reaction in CoSAC@CNT/S. Galvanostatic charge/discharge patterns were additionally measured at a current rate of 0.1C, where 1C is equivalent to 1675 mA g$^{-1}$. Fig. 5c shows that the red/ox peaks in the CV curves were in agreement with the charge and discharge levels. The investigated capacity of the Li–S cell which was fabricated from the CoSAC@CNT/S composite was 1346 mA h g$^{-1}$, which was significantly greater than those of the Li–S cells made from the CoNP@CNT/S composite (1254 mA h g$^{-1}$) and the CNT/S composite (1169 mA h g$^{-1}$). Taken together, all of these findings suggested that the Co SACs included within the CoSAC@CNT/S could speed up the sulfur conversion reaction.

Among the three tested cathodes, it was observed that the cathodes containing CoSAC@CNT/S constantly showed the highest specific capacity (Fig. 5d). For example, the unique capability achieved by the CoNP@CNT/S cathode at 3C was higher compared to the values obtained for the CoNP@CNT/S and CNT/S cathodes (650 mA h g$^{-1}$ *versus* 580 and 500 mA h g$^{-1}$ respectively). This was the case because the CoSAC@CNT/S cathode had a higher active site. In the case of the CoSAC@CNT/S cathode, a specific capacity of 1150 mA h g$^{-1}$ was recorded when the current rate was restored to 0.2C. The similarity of the value to the initial value of 1160 mA h$^{-1}$ suggests that there is a notable level of reversibility in the CoSAC@CNT/S cathode. After undergoing 60 consecutive cycles, a specific capacity of 1160 mA h g$^{-1}$ was observed, indicating a remarkable capacity retaining rate of 97%. The significant retention of capability and capacity rates of the CoSAC@CNT/S cathode were mainly attributed to the implanted Co single atoms that stimulate the reaction process of Li–S cell cathodes. Fig. 5e displays the galvanostatic charge/discharge patterns of the cathode composed of CoSAC@CNT/S. The potential gradient ($E$) observed during the charge/discharge plateau is indicative of the polarization of the electrode. The profiles were obtained at current rates varying from 0.2C to 6C.[72] The CoSAC@CNT/S cathode demonstrated the ability to maintain a consistent charge/discharge plateau despite an increase in the current rate, unlike the galvanostatic profiles observed for the CoNP@CNT/S and CNT cathodes (Fig. S4†). Fig. 5e demonstrates that at high current densities, the $E$ of the CoSAC@CNT/S cathode was continually smaller than that of CoNP@CNT/S or CNT cathodes (0.66 V, 0.87 V, and 1.10 V, respectively). The electrocatalytic activity supplied by the Co SACs was responsible for the smaller polarization measured at the CoSAC@CNT/S cathode, which suggested quicker reaction kinetics. In this regard, the overpotential of CoSAC@CNT/S is 24 mV, which is lower than that of CoNP@CNT/S (34 mV) and CNT (32 mV), respectively. The decreased overpotential facilitates faster Li$_2$S deposition owing to the minimized interfacial energy barrier, primarily arising from the efficient adsorption/diffusion/transformation process of LiPSs on the catalyst. This enhancement is crucial for promoting sulfur utilization and suppressing the shuttle effect. Noteworthily the initial potential of CoSAC@CNT/S (1.74 V) is also lower than that of CoNP@CNT/S (1.77 V) and CNTs (2.17 V), which specifies that more polysulfides could be formed while contributing to capacity. Furthermore, CoSAC@CNT/S demonstrates an extended active period and enhanced Li$_2$S activity, providing additional evidence that the increased polysulfide synthesis contributes to the improved capacity. High capacity with little capacity fading is displayed by the CoSAC@CNT/S electrode, as illustrated in Fig. 5f. Additionally, measurement of the high sulfur loading is an important metric for assessing the energy density of operational Li–S batteries. Thus, electrodes with increased sulfur loading were investigated to take advantage of the improved conversion kinetics and the subsequent reduction in the shuttle effect. Sulfur areal loading was elevated to approximately 7 mg cm$^{-2}$. In the beginning, the batteries became active by cycling at a rate of 0.05C for the preliminary three cycles. For the following runs, the cycling rate was increased to 0.2C. When the bulk loading rises to 5 mg cm$^{-2}$ and 7 mg cm$^{-2}$, the respective capacities are 4.8 and 4.0 mA h cm$^{-2}$. Even when subjected to a high amount of loaded sulfur, the electrode exhibits durable and stable function with a high capacity preservation, proving the value of the synergistic role of CoSAC@CNT/S in polysulfides absorption and conversion (Fig. 5g). To assess the long-term cycling stability of Li–S cells, rigorous testing was conducted at a current rate of 1C. This approach was chosen as the sulfur species' shuttle effect is particularly prominent at lower current rates. The CoSAC@CNT/S cathode initially showed a specific capacity of 1200 mA h g$^{-1}$, which remained stable at 990 mA h g$^{-1}$ even after undergoing 1000 cycles (Fig. 5h). This represents a minimal capacity decline of only 0.08% per cycle. The capacity loss for both CoNP@CNTs and CNT/S is measured to be 0.052% and 0.049%, respectively. The active absorption and transformation of sulfur species in CoSAC@CNT/S is supported by the high capacity retention observed. This can be attributed to the highly active surface of the CoSAC@CNT/S host and the good charge transfer ability on the CoSAC@CNT/S polysulfide interface.

## Conclusion

To sum up, we have introduced a new method for synthesising single cobalt atoms immobilised on a CNT matrix using PPy/PANI precursors. This composite material can be used to create lithium–sulfur batteries (LSBs) by providing a sulphur cathode with a robust and electrochemically active host. Precipitation experiments with Li$_2$S and a series of measurements utilising symmetrical and asymmetrical cells were part of the experimental inquiry. The findings showed that when compared to control electrodes that had CoNP/CNT nanoparticles present, electrodes with CoSAC/CNT showed higher Li$^+$ diffusion coefficients and a larger degree of Li$_2$S deposition. Utilising CoSAC/CNT as a sulphur host during fabrication, the Li–S cells demonstrated exceptional performance attributes. A few of these are a

significant rate capacity of 810 mA h g$^{-1}$ at a rate of 6C, an exceptionally high specific capacity of 1346 mA h g$^{-1}$ at a rate of 0.1C, and remarkable cycling stability with a capacity of 990 mA h g$^{-1}$ at a rate of 1C after 1000 cycles. This translates to a negligible 0.08% degradation rate per cycle. The study's results provide new insights into the electrocatalytic processes taking place in Li–S cell sulphur cathodes. Furthermore, the presented methodology offers a general framework for adjusting other single-atom catalysts (SACs) for usage in contemporary electrocatalytic processes.

## Author contributions

Khalida Abaid Samawi: resources. Ekhlas Abd-Alkuder Salman: investigation. Hiba Ali Hasan: funding acquisition. HassabAlla M. A. Mahmoud: methodology, investigation. G. Abdulkareem-Alsultan & Emilia Abdulmalek: reviewing & editing. Maadh Fawzi Nassar: methodology, investigation, conceptualization, validation, writing – original draft, writing – review & editing.

## Conflicts of interest

The authors state that none of their known financial conflicts or interpersonal connections might have had an impact on the work presented in this paper.

## Acknowledgements

## References

1 P. Akbarian, M. Kheirmand and M. Faraji, Facile electrochemical fabrication of high-performance graphene quantum dots-supported Mn3O4/Ag hybrid catalyst for oxygen reduction reaction in alkaline media, *Int. J. Energy Res.*, 2022, **46**(15), 23004–23019.

2 H. Gharibi, M. Faraji and M. Kheirmand, The Role of PANI/Nafion on the Performance of ORR in Gas Diffusion Electrodes of PEM Fuel Cell, *Electroanalysis*, 2012, **24**(12), 2354–2364.

3 M. Faraji and S. Moradi Dehaghi, Pd-doped g-C$_3$N$_4$ decorated by nitrogen-doped carbon quantum dot as a high performance electrocatalyst with superior durability and methanol tolerance for oxygen reduction reaction, *Inorg. Chem. Commun.*, 2021, **123**, 108328.

4 R. Zhang, *et al.*, NiCo-LDH/Ti$_3$C$_2$ MXene hybrid materials for lithium ion battery with high-rate capability and long cycle life, *J. Energy Chem.*, 2020, **50**, 143–153.

5 J. Shi, *et al.*, Ultrathin Ni-Co double hydroxide nanosheets with conformal graphene coating for highly active oxygen evolution reaction and lithium ion battery anode materials, *Chem. Eng. J.*, 2017, **327**, 9–17.

6 E. Abd-Alkuder Salman, *et al.*, 3D Hollow Spheres Comprising MXene/g-C$_3$N$_4$ Heterostructre for Efficient Polysulfide Adsorption and Conversion in High-Performance Li–S Batteries, *J. Electroanal. Chem.*, 2023, 117629.

7 M.-Q. Zhao, *et al.*, Hollow MXene Spheres and 3D Macroporous MXene Frameworks for Na-Ion Storage, *Adv. Mater.*, 2017, **29**(37), 1702410.

8 Q. Shao, S. Zhu and J. Chen, A review on lithium-sulfur batteries: Challenge, development, and perspective, *Nano Res.*, 2023, **16**(6), 8097–8138.

9 K. Zhang, *et al.*, Oxygen vacancies in open-hollow microcapsule enable accelerated kinetics for stable Li–S battery, *J. Colloid Interface Sci.*, 2023, **629**, 805–813.

10 Z. Yang, *et al.*, Multi-function hollow nanorod as an efficient sulfur host accelerates sulfur redox reactions for high-performance Li–S batteries, *J. Colloid Interface Sci.*, 2023, **629**, 65–75.

11 S. H. Yang, *et al.*, Hollow porous carbon nanospheres containing polar cobalt sulfide (Co9S8)A nanocrystals as electrocatalytic interlayers for the reutilization of polysulfide in lithium–sulfur batteries, *J. Colloid Interface Sci.*, 2023, **645**, 33–44.

12 J. Xiong, *et al.*, Modified separators boost polysulfides adsorption-catalysis in lithium-sulfur batteries from Ni@Co hetero-nanocrystals into CNT-porous carbon dual frameworks, *J. Colloid Interface Sci.*, 2023, **652**, 1417–1426.

13 D. Liu, *et al.*, Electrospun CuCoN0.6 coating necklace-like N-doped carbon nanofibers for high performance lithium-sulfur batteries, *J. Colloid Interface Sci.*, 2023, **645**, 705–714.

14 Z. Kong, *et al.*, Cobalt nanoparticles & nitrogen-doped carbon nanotubes@hollow carbon with high catalytic ability for high-performance lithium sulfur batteries, *J. Colloid Interface Sci.*, 2023, **648**, 846–854.

15 G. Cao, R. Duan and X. Li, Controllable catalysis behavior for high performance lithium sulfur batteries: From kinetics to strategies, *EnergyChem*, 2023, **5**(1), 100096.

16 Q. Wu, *et al.*, Carbon-based derivatives from metal-organic frameworks as cathode hosts for Li–S batteries, *J. Energy Chem.*, 2019, **38**, 94–113.

17 Z. Huang, *et al.*, High-Energy Room-Temperature Sodium–Sulfur and Sodium–Selenium Batteries for Sustainable Energy Storage, *Electrochem. Energy Rev.*, 2023, **6**(1), 21.

18 Z. Li, *et al.*, Correlating Polysulfide Solvation Structure with Electrode Kinetics towards Long-Cycling Lithium–Sulfur Batteries, *Am. Ethnol.*, 2023, **135**(43), e202309968.

19 Y. Liu, *et al.*, An organodiselenide comediator to facilitate sulfur redox kinetics in lithium–sulfur batteries with encapsulating lithium polysulfide electrolyte, *Am. Ethnol.*, 2023, **62**(30), e202303363.

20 Z.-X. Chen, *et al.*, Cathode kinetics evaluation in lean-electrolyte lithium–sulfur batteries, *J. Am. Chem. Soc.*, 2023, **145**(30), 16449–16457.

21 L. Li, *et al.*, Rational design of a well-aligned metal–organic framework nanopillar array for superior lithium-sulfur batteries, *Chem. Eng. J.*, 2023, **454**, 140043.

22 H. Raza, *et al.*, Li–S Batteries: Challenges, Achievements and Opportunities, *Electrochem. Energy Rev.*, 2023, **6**(1), 29.

23 K. Wang, *et al.*, The Single-atom site Catalysis in Li–S batteries, *Phys. Chem. Chem. Phys.*, 2023, **25**, 25942–25960.

24 S. Yang, *et al.*, Recent advances in cathodes for all-solid-state lithium-sulfur batteries, *Chin. Chem. Lett.*, 2023, **34**(7), 107783.

25 J. Wang, *et al.*, Advances in single metal atom catalysts enhancing kinetics of sulfur cathode, *Acta Phys.-Chim. Sin.*, 2023, **39**(5), 2212005.

26 Y. Song, *et al.*, Rationalizing the impact of oxygen vacancy on polysulfide conversion kinetics for highly efficient lithium-sulfur batteries, *J. Energy Chem.*, 2023, **87**, 51–60.

27 P. Feng, *et al.*, Ultrathin two-dimensional bimetal NiCo-based MOF nanosheets as ultralight interlayer in lithium-sulfur batteries, *Chin. Chem. Lett.*, 2023, **34**(4), 107427.

28 Y. Wang, *et al.*, Oxygen self-doping pyrolyzed polyacrylic acid as sulfur host with physical/chemical adsorption dual function for lithium-sulfur batteries, *Chin. Chem. Lett.*, 2023, 109001.

29 X. Sun, *et al.*, Emerging multifunctional iron-based nanomaterials as polysulfides adsorbent and sulfur species catalyst for lithium-sulfur batteries—A mini-review, *Chin. Chem. Lett.*, 2023, **34**(1), 107501.

30 S. Jiang, *et al.*, Bimetal-organic frameworks derived Co/N-doped carbons for lithium-sulfur batteries, *Chin. Chem. Lett.*, 2020, **31**(9), 2347–2352.

31 Z. Liu, L. Wang and W. Yang, Hierarchically porous nitrogen-doped carbon foams decorated with zinc nanodots as high-performance sulfur hosts for lithium-sulfur battery, *Chin. Chem. Lett.*, 2021, **32**(9), 2919–2922.

32 H. Zhang, *et al.*, A rational design of titanium-based heterostructures as electrocatalyst for boosted conversion kinetics of polysulfides in Li–S batteries, *J. Colloid Interface Sci.*, 2023, **633**, 432–440.

33 G. Wen, *et al.*, An interwoven carbon nanotubes/cerium dioxide electrocatalyst accelerating the conversion kinetics of lithium sulfide toward high-performance lithium-sulfur batteries, *J. Colloid Interface Sci.*, 2022, **623**, 697–702.

34 D. Wang, *et al.*, Sulfur-deficient MoS2-carbon hollow nanospheres for synergistic trapping and electrocatalytic conversion of polysulfides, *J. Colloid Interface Sci.*, 2023, **630**, 535–543.

35 H. Qiu, *et al.*, Three-dimensional carbon foam decorated with SnO2 as multifunctional host for lithium sulfur batteries, *J. Colloid Interface Sci.*, 2023, **630**, 106–114.

36 M. Li, *et al.*, FeCo/Fe3C-cross-linked N-doped carbon via synergistic confinement and efficient catalyst to enable high-performance Li–S batteries, *J. Colloid Interface Sci.*, 2022, **628**, 54–63.

37 Y. Song, X. Li and C. He, Porous carbon framework nested nickel foam as freestanding host for high energy lithium sulfur batteries, *Chin. Chem. Lett.*, 2021, **32**(3), 1106–1110.

38 F. Wang, *et al.*, Single-Atom Electrocatalysts for Lithium Sulfur Batteries: Progress, Opportunities, and Challenges, *ACS Mater. Lett.*, 2020, **2**(11), 1450–1463.

39 Y. Song, *et al.*, Single-atom electrocatalysts for lithium–sulfur chemistry: Design principle, mechanism, and outlook, *Carbon Energy*, 2023, **5**(4), e286.

40 Y. Miao, *et al.*, Synthesis and application of single-atom catalysts in sulfur cathode for high-performance lithium–sulfur batteries, *Chin. Chem. Lett.*, 2023, **34**(1), 107121.

41 T. Zhou, *et al.*, Fundamental, application and opportunities of single atom catalysts for Li–S batteries, *Energy Storage Mater.*, 2023, **55**, 322–355.

42 Y. Wang, *et al.*, Single Atom Catalysts for Fuel Cells and Rechargeable Batteries: Principles, Advances, and Opportunities, *ACS Nano*, 2021, **15**(1), 210–239.

43 Z. Liang, *et al.*, Advances in the Development of Single-Atom Catalysts for High-Energy-Density Lithium–Sulfur Batteries, *Adv. Mater.*, 2022, **34**(30), 2200102.

44 Y. Li, *et al.*, Fast conversion and controlled deposition of lithium (poly)sulfides in lithium-sulfur batteries using high-loading cobalt single atoms, *Energy Storage Mater.*, 2020, **30**, 250–259.

45 Y. Li, *et al.*, Cobalt single atoms supported on N-doped carbon as an active and resilient sulfur host for lithium–sulfur batteries, *Energy Storage Mater.*, 2020, **28**, 196–204.

46 X. Meng, *et al.*, Single-Atom Catalyst Aggregates: Size-Matching is Critical to Electrocatalytic Performance in Sulfur Cathodes, *Adv. Sci.*, 2022, **9**(3), 2103773.

47 Z. Zeng, *et al.*, Universal-Descriptors-Guided Design of Single Atom Catalysts toward Oxidation of Li2S in Lithium–Sulfur Batteries, *Adv. Sci.*, 2021, **8**(23), 2102809.

48 M. Xie, *et al.*, Single-atom Co-N5 catalytic sites on carbon nanotubes as peroxymonosulfate activator for sulfamerazine degradation via enhanced electron transfer pathway, *Sep. Purif. Technol.*, 2023, **304**, 122398.

49 N. Ma, *et al.*, Curvature effects regulate the catalytic activity of Co@N4-doped carbon nanotubes as bifunctional ORR/OER catalysts, *J. Colloid Interface Sci.*, 2024, **654**, 1458–1468.

50 S.-H. Lin, *et al.*, Cobalt Sulfide Nanoparticles Embedded Carved Carbon Nanoboxes Dispersed in Iron Single-Atom decorated Multiwalled Carbon Nanotube Porous Structure as a Host Material for Lithium–Sulfur Batteries, *ACS Sustainable Chem. Eng.*, 2023, **11**(31), 11645–11659.

51 M. Ma, *et al.*, Tailoring FeP with a Hollow Urchin Architecture for High-Performance Li–S Batteries, *ACS Sustainable Chem. Eng.*, 2021, **9**(15), 5315–5321.

52 Y. Wang, *et al.*, CoN4 active sites in locally distorted carbon structure for efficient oxygen reduction reaction via regulating coordination environment, *Chem. Eng. J.*, 2022, **429**, 132119.

53 J. Yang, *et al.*, Compressive strain modulation of single iron sites on helical carbon support boosts electrocatalytic oxygen reduction, *Angew. Chem., Int. Ed.*, 2021, **60**(42), 22722–22728.

54 Q. Lu, *et al.*, Single-crystal inorganic helical architectures induced by asymmetrical defects in sub-nanometric Wires, *J. Am. Chem. Soc.*, 2021, **143**(26), 9858–9865.

55 D. Hursán, *et al.*, Morphological attributes govern carbon dioxide reduction on N-doped carbon electrodes, *Joule*, 2019, **3**(7), 1719–1733.

56 A. S. Andreev, *et al.*, Magnetic and dielectric properties of carbon nanotubes with embedded cobalt nanoparticles, *Carbon*, 2017, **114**, 39–49.

57  Z. Xu, *et al.*, Atomically dispersed cobalt in core-shell carbon nanofiber membranes as super-flexible freestanding air-electrodes for wearable Zn-air batteries, *Energy Storage Mater.*, 2022, **47**, 365–375.

58  S. Gu, *et al.*, Electrostatic Potential-Induced Co–N4 Active Centers in a 2D Conductive Metal–Organic Framework for High-Performance Lithium–Sulfur Batteries, *ACS Appl. Mater. Interfaces*, 2022, **14**(45), 50815–50826.

59  X. Tao, *et al.*, Engineering MOFs-Derived Nanoarchitectures with Efficient Polysulfides Catalytic Sites for Advanced Li–S Batteries, *Adv. Mater. Technol.*, 2023, **8**(2), 2200238.

60  A. M. Hibberd, *et al.*, Co polyoxometalates and a Co3O4 thin film investigated by L-edge X-ray absorption spectroscopy, *J. Phys. Chem. C*, 2015, **119**(8), 4173–4179.

61  Y. Han, *et al.*, Hollow N-doped carbon spheres with isolated cobalt single atomic sites: superior electrocatalysts for oxygen reduction, *J. Am. Chem. Soc.*, 2017, **139**(48), 17269–17272.

62  L. Liu and A. Corma, Metal catalysts for heterogeneous catalysis: from single atoms to nanoclusters and nanoparticles, *Chem. Rev.*, 2018, **118**(10), 4981–5079.

63  X. X. Wang, *et al.*, Nitrogen-Coordinated Single Cobalt Atom Catalysts for Oxygen Reduction in Proton Exchange Membrane Fuel Cells, *Adv. Mater.*, 2018, **30**(11), 1706758.

64  G. Wu, *et al.*, Synthesis–structure–performance correlation for polyaniline–Me–C non-precious metal cathode catalysts for oxygen reduction in fuel cells, *J. Mater. Chem.*, 2011, **21**(30), 11392–11405.

65  H. Tian, *et al.*, High-power lithium–selenium batteries enabled by atomic cobalt electrocatalyst in hollow carbon cathode, *Nat. Commun.*, 2020, **11**(1), 5025.

66  D. Vanderbilt, Soft self-consistent pseudopotentials in a generalized eigenvalue formalism, *Phys. Rev. B*, 1990, **41**(11), 7892.

67  Z. Ye, *et al.*, A high-efficiency CoSe electrocatalyst with hierarchical porous polyhedron nanoarchitecture for accelerating polysulfides conversion in Li–S batteries, *Adv. Mater.*, 2020, **32**(32), 2002168.

68  R. Sun, *et al.*, Enhancing polysulfide confinement and electrochemical kinetics by amorphous cobalt phosphide for highly efficient lithium–sulfur batteries, *ACS Nano*, 2020, **15**(1), 739–750.

69  Q. Pang, *et al.*, A nitrogen and sulfur dual-doped carbon derived from Polyrhodanine@ Cellulose for advanced lithium–sulfur batteries, *Adv. Mater.*, 2015, **27**(39), 6021–6028.

70  X. Liang, *et al.*, Interwoven MXene nanosheet/carbon-nanotube composites as Li–S cathode hosts, *Adv. Mater.*, 2017, **29**(3), 1603040.

71  X. Liang, *et al.*, A highly efficient polysulfide mediator for lithium–sulfur batteries, *Nat. Commun.*, 2015, **6**(1), 5682.

72  G. Zhou, *et al.*, Theoretical calculation guided design of single-atom catalysts toward fast kinetic and long-life Li–S batteries, *Nano Lett.*, 2019, **20**(2), 1252–1261.